Chemical Engineering Journal 459 (2023) 141573

Contents lists available at ScienceDirect

Chemical Engineering Journal

journal homepage: www.elsevier.com/locate/cej

Simultaneous defect passivation and energy level modulation by multifunctional phthalocyanine for efficient and stable perovskite solar cells

Jiawei Zhang [a,b], Tie Liu [a,*], Zhiqiang Bao [a,b], He Liu [a,b], Ying Lv [a], Xiaoyang Guo [a], Xingyuan Liu [a], Yulei Chang [a], Bin Li [a,b,c,*]

[a] State Key Laboratory of Luminescence and Applications, Changchun Institute of Optics, Fine Mechanics and Physics, Chinese Academy of Sciences, Changchun 130033, PR China

[b] University of Chinese Academy of Sciences, Beijing 100049, PR China

[c] Center of Materials Science and Optoelectronics Engineering, University of Chinese Academy of Sciences, Beijing 100049, PR China

ARTICLE INFO

Keywords:
$MAPbI_3$
Phthalocyanine
Energy level
Defect passivation
Perovskite solar cells

ABSTRACT

Interface passivation is an effective means to decrease detrimental defects and realize highly efficient and stable perovskite solar cells (PSCs). Nevertheless, most of the interfacial passivators currently used are easily formed mismatched energy levels and impede the extraction of photogenerated charge carriers. Herein, a metal-free H_2-phthalocyanine (H_2Pc) is reported to passivate the interface defects and improve the crystallinity and energy level alignment. Contrasting metal Zn-phthalocyanine, the pyrrolic nitrogen and N—H bond in the structure of the H_2Pc molecule exhibit a higher capability to interact with unsaturated Pb and I site. It is found that the defects passivation and improved crystallinity in H_2Pc molecule treatment are achieved by the formation of coordination bonding between N atoms and uncoordinated Pb^{2+} ions and hydrogen bonding between N—H bond and I (iodine). Simultaneously, the H_2Pc treatment can also improve energy level alignment and promote the charge extraction from perovskite to the hole transport material layer. As a result, a champion power conversion efficiency (PCE) of 20.59 % is achieved for the H_2Pc PSCs, which is higher than that of 18.54 % for the ZnPc PSCs and 16.50 % for the pristine PSCs. Meanwhile, the H_2Pc device shows significantly improved moisture, thermal, and illumination stability and with retaining over 90 % of its initial PCE after aging for 1000 h at about 20 % relative humidity in ambient conditions. The present work provides a practical and efficient method of simultaneous defect passivation and energy level modulation and toward the purpose of attaining superior performance PSCs and other perovskite-based electronics.

1. Introduction

Organic–inorganic hybrid perovskite materials have acquired a premier reputation in next-generation photovoltaics due to their outstanding optical and electronic characteristics, such as tunable bandgap, low exciton binding energy, high extinction coefficient, and excellent ambipolar carrier transport property [1–4]. Over the past decade, the power conversion efficiency (PCE) of perovskite solar cells (PSCs) has rapidly increased from 3.8 % to 25.7 %, which approaches the record PCE of traditional crystalline silicon solar cells [5–7]. Despite substantial advances, there is also a certain gap between the present PCE and Shockley − Queisser limit, and the long-term stability of PSCs is still an obstacle to the entry into the commercial photovoltaic market. The stability issues arising from extrinsic factors such as moisture and oxygen can be overcome by encapsulation methods, while the encapsulating technique is unable to solve that resulting from intrinsic defects and thermal degradation. It has been widely demonstrated that most of the perovskite degradations are initialized from the interfaces and grain boundaries owing to the high defect density [8–10]. And both defects at the bulk and surface can induce ion migration and charge accumulation under the work condition with light illumination and an electric field which severely accelerate the degradation of perovskite [11,12].

* Corresponding authors at: State Key Laboratory of Luminescence and Applications, Changchun Institute of Optics, Fine Mechanics and Physics, Chinese Academy of Sciences, Changchun 130033, PR China.

E-mail addresses: liutie@ciomp.ac.cn (T. Liu), lib020@ciomp.ac.cn (B. Li).

https://doi.org/10.1016/j.cej.2023.141573
Received 5 November 2022; Received in revised form 3 January 2023; Accepted 25 January 2023
Available online 27 January 2023

Moreover, these defects (including dangling bonds [8], uncoordinated ions [13], lead clusters [14], etc.) also trap free charge carriers and subsequently annihilated with oppositely charged carriers by acting as nonradiative recombination centers, which dramatically impair the efficiency of PSCs. Therefore, the passivation of defects in perovskite materials is the most important prerequisite for obtaining highly efficient and stable PSCs.

Up to now, multifarious defect passivation methods have been employed to improve the performance of PSCs, including inorganic compounds [15–17], small organic molecules [18–21], polymers [22–24], and low-dimensional perovskites [25–27]. In 2019, Huang *et al.* converted the surfaces of lead halide perovskite to wide-bandgap lead oxysalt layers by post-treating with sulfate or phosphate ions, which passivated the undercoordinated Pb clusters and stabilized the operation of PSCs [8]. In 2021, Wu *et al.* introduced a cross-linked polysilane between the perovskite and hole transport layer, and the formation of the discontinuous dielectric interlayer remarkably reduced the charge recombination loss and significantly improved the performance of PSCs [28]. Moreover, the formation of 2D perovskites on top of 3D counterparts is also an effective approach to passivate the defects. The large organic ammonium cations such as *n*-butylammonium (BA^+) [29,30], phenethylammonium (PEA^+) [31], and cyclohexylethylammonium (CEA^+) [32] have been applied to convert the perovskite structure from 3D to 2D, which effectively enhance the stability of the corresponding PSCs. However, most of the defect passivation methods introduce electrically insulating layers and mismatch band alignments which leads to an unfavorable charge transport and brings an impeditive effect on the further performance enhancement of PSCs. Thereby, it is highly urgent to explore a multifunctional passivation material with high charge transport ability, appropriate energy levels, and high stability.

Phthalocyanine (*Pc*) is an organic p-type small molecule semiconductor, which has been widely applied in dye-sensitized solar cells as a sensitizer and organic photovoltaic cells as a donor material, because of its unique properties such as broad light absorption, high hole mobility, and high moisture, thermal, and chemical stability [33–35]. Most recently, the *Pc* derivatives have also been used as hole transporting materials and interfacial modifying materials in PSCs. Xu et al. reported methylthiotriphenylamine-substituted copper phthalocyanine (SMe-TPACuPc) as a dopant-free hole transporting material, which not only improves the thermal stability of PSCs but also passivates the uncoordinated Pb^{2+} ion defects on the surface of perovskite [36]. Cao et al. employed tetra-ammonium zinc phthalocyanine to post-treat $MAPbI_3$ film to construct (2D) $(ZnPc)_{0.5}MA_{n-1}Pb_nI_{3n+1}$ perovskite phase, which gives the function of grain boundary suture [34]. Moreover, the tetra-*tert*-butyl copper phthalocyanine and nickel phthalocyanine were also introduced as modified agents to improve the performance of PSCs [37,38]. However, the complex function of the *Pc* molecule on device performance improvement is still vague, and the lack of in-depth understanding on modulation mechanisms prevents their applications in PSCs.

In this study, both metal-free *Pc* and metal *Pc* were presented to improve the performance of PSCs. It found that the pyrrole unit inner rings in the structure of metal-free tetra(*tert*-butyl) H_2-phthalocyanine (H_2Pc) molecule exhibit higher interaction capability with unsaturated Pb and I site than that of metal tetra(*tert*-butyl) Zinc phthalocyanine (ZnPc) molecule. Equally importantly, the H_2Pc-treated perovskite also shows improved energy level alignment with adjacent SpiroOMeTAD layers, and exceptional hydrophobicity and charge transport ability. As a result, the H_2Pc device shows a champion PCE of 20.59 %, which is higher than that of ZnPc and pristine device. And benefited from the hydrophobicity property and thermal stability of *Pc* molecule, the stability against moisture and thermal were significantly improved by the H_2Pc treatment.

2. Results and discussion

The device configuration adopted in this work is illustrated in Fig. 1a. To improve the performance of PSCs, the defect passivation is conducted by premixing appropriate amounts of H_2Pc or ZnPc molecules into the chlorobenzene antisolvent and dropping it on samples during the one-step deposition process. The molecular structures of ZnPc and H_2Pc molecules are exhibited in Fig. S1. The bottom of Fig. 1a presents the cross-sectional SEM image of a full device based on H_2Pc treated perovskite, where we can observe that a well-defined multilayer structure without any gaps is fitted tightly on the FTO substrate, and the thickness of the perovskite layer is estimated to be 350 nm. The surface electrostatic potential (ESP) maps and energy levels of *Pc* molecules are investigated by density functional theory (DFT) calculations. As shown in Fig. 1b and 1c, the H_2Pc molecule exhibits a higher negative charge density on nitrogen atoms of pyrrole rings compared with the ZnPc molecule, which provides more favorable conditions for coordination with uncoordinated Pb^{2+} ion. The possible passivation mechanism is schematically depicted in Fig. 1c. Both the pyrrolic nitrogen and linked nitrogen (pyrrole rings are linked by nitrogen atoms) spontaneously donate their lone pair electrons to the empty 6p orbital of unsaturated Pb via coordination interactions, eliminating iodine vacancy defects and relaxing the distortions of octahedral structure according to the classical Jahn-Teller effect. And the hydrogen bonding can be formed between N—H bonds in H_2Pc molecule and I (iodine) in perovskite which may assist the primary nitrogen atoms binding with the Pb defects [39,40]. The detailed interaction modes and passivation mechanism will be analyzed and proved in the characterization section. Besides the minimization of trap states, optimizing the energy level alignment at the perovskite/HTM interface is equally important to reduce trap-assisted interfacial recombination by ensuring charge extraction efficiency. The highest occupied molecular orbital (HOMO) and lowest unoccupied molecular orbital (LUMO) are calculated to be −4.77 and −2.64 eV for the ZnPc molecule and −4.81 and −2.69 eV for the H_2Pc molecule, respectively, as presented in Fig. S2. It is worth noting that the HOMO levels of both *Pc* molecules are higher than the valence band of perovskite and the HOMO level of the H_2Pc molecule is deeper than that of the ZnPc molecule which is beneficial for better energy level alignment to reduce V_{oc} loss [41,42]. To evaluate the effect of H_2Pc treatment on the surface band structures, ultraviolet photoelectron spectrometry (UPS) and UV–vis absorption spectrum measurements were conducted. As shown in Fig. 1d, the secondary electron cutoff edges (E_{cutoff}) of pristine and H_2Pc-treated perovskite are 16.91 eV and 17.30 eV, respectively. According to the formula $-E_F = 21.22 - E_{cutoff}$, the Fermi level ($E_F$) values are calculated to be −4.31 eV and −3.92 eV, respectively. As shown in valence band region of UPS spectra (Fig. 1e), the values of $E_F - E_{VBM}$ (maximum of valence band) are determined to be 1.43 eV and 1.37 eV, respectively. Therefore, the E_{VBM} for pristine and H_2Pc perovskite are calculated as − 5.74 eV and − 5.29 eV, respectively. Combination with the Tauc plots derived from UV–vis absorption spectra as shown in Fig. 3f and Fig. S3a, b, the conduction band minimum (E_{CB}) values are calculated to be −4.12 eV and −3.67 eV for the pristine and H_2Pc perovskite, respectively, and the detailed energy level diagrams are shown in Fig. S3c. And Fig. 1f presents the energy level diagram of the PSCs and the energy level diagram of H_2Pc and ZnPc molecules, wherein the energy level of TiO_2 and SpiroOMeTAD is referred to previous reports [43,44]. It is worth noting that the H_2Pc-treated perovskite shows a better valence band alignment to SpiroOMeTAD, which is conducive to hole extraction and transport, and reducing the energy loss at the HTL/perovskite interface. Furthermore, the *Pc* treatments are mainly targeting the surface of perovskite and may not participate into the bottom of the perovskite crystal due to the steric hindrance effect of the large molecules [41,45]. Thus, the energy level of the underlying perovskite is not changed, which results in a stepwise energy level structure as exhibited in Fig. 1f.

To confirm the interaction between the perovskites and *Pc*

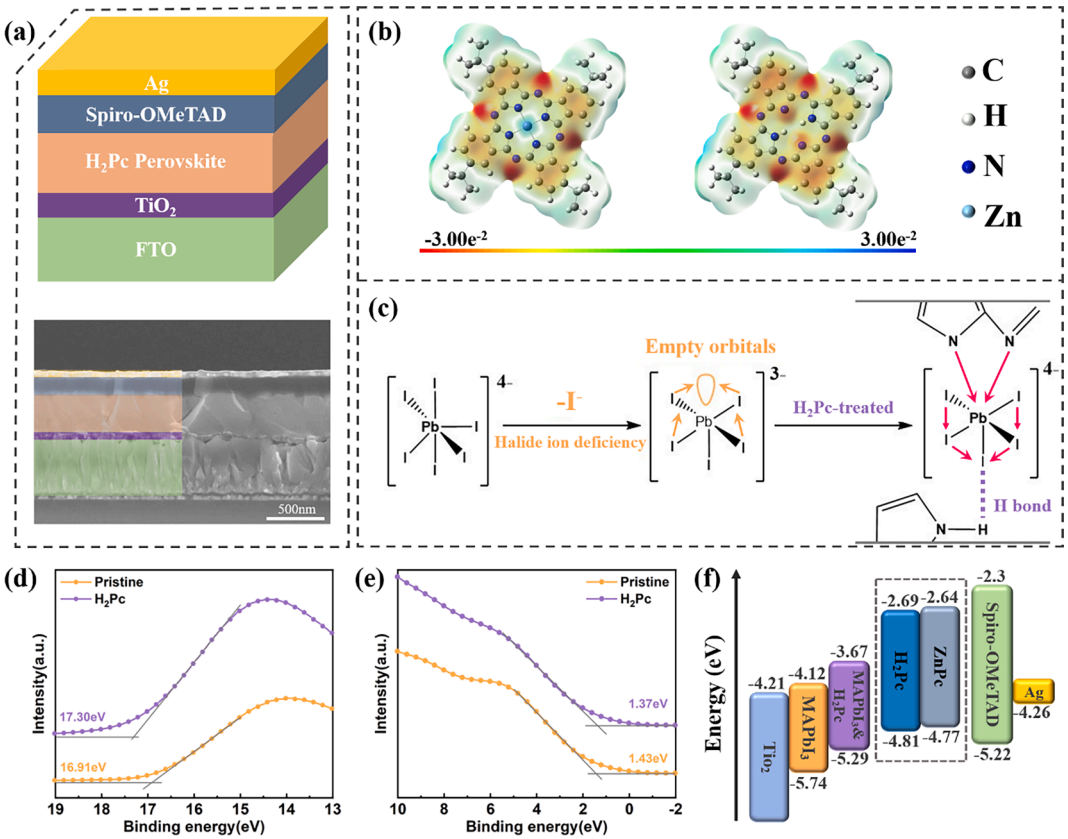

Fig. 1. (a) Schematic device structure adopted in this work and cross-sectional SEM image of a full device employing H_2Pc treated perovskite as photoactive layer. (b) Calculated ESP maps of H_2Pc and ZnPc molecules. (c) Schematic illustration of defect passivation by H_2Pc molecule. (d)-(e) The secondary electron cutoff region and valence band region of UPS spectra of pristine and H_2Pc perovskite. (f) The energy level diagram in PSCs and energy level diagram of H_2Pc and ZnPc molecules.

molecules, the Fourier transform infrared (FTIR) spectra were carried out. As shown in Fig. 2a, the ZnPc sample shows two peaks at 1664 cm^{-1} and 1527 cm^{-1}, which are assigned to the stretching vibration of the C═N bond and the aromatic ring skeleton [13,39]. These two peaks are shifted to lower wavenumbers of 1622 cm^{-1} and 1470 cm^{-1} in ZnPc-PbI_2 sample, which demonstrates the formation of coordination

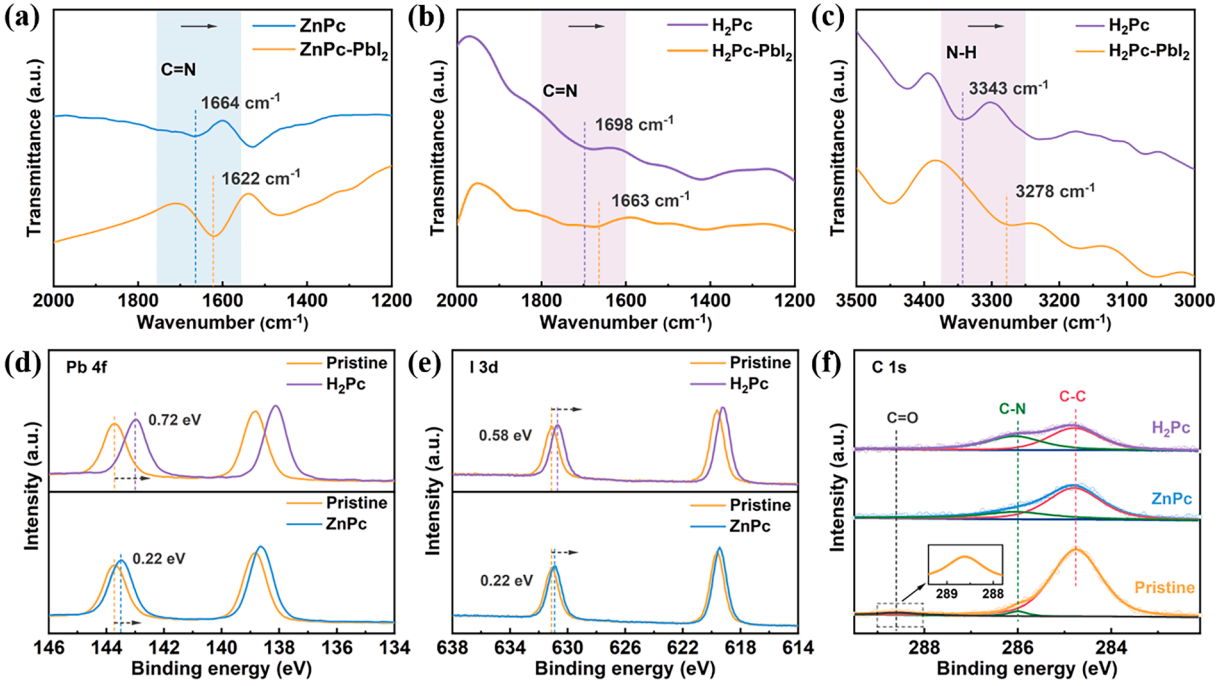

Fig. 2. FTIR spectra of (a) ZnPc and ZnPc/PbI_2 films, (b)-(c) H_2Pc and H_2Pc/PbI_2 films. XPS core-level spectra of (d) Pb 4f, (e) I 3d, and (f) C 1 s for pristine, ZnPc-treated and H_2Pc-treated perovskite films.

interaction between pyrrole nitrogen and uncoordinated Pb^{2+}. The shift of the aromatic ring skeleton stretching vibration peak is attributed to the electron transfer between nitrogen atoms and the aromatic ring skeleton, which is resulted from the formation of coordination interaction between pyrrole nitrogen and uncoordinated Pb^{2+}. Similar variation shifts can also be observed in H_2Pc-PbI_2 film as shown in Fig. 2b, the peak at 1698 cm^{-1} in H_2Pc molecule shifts to a lower wavenumber of 1663 cm^{-1} in H_2Pc-PbI_2 film, which is also attributed to the coordination interaction between C═N in H_2Pc molecule and uncoordinated Pb^{2+} in the perovskite. Moreover, the pure H_2Pc shows a higher wavenumber of N—H bond at 3343 cm^{-1} than that of H_2Pc-PbI_2 mixture films at 3278 cm^{-1} as shown in Fig. 2c. This is may be ascribed to the formation of hydrogen bond between the N—H bond and I, which leads to the electron delocalization of H_2Pc molecules and reduces the corresponding vibration frequency [16,39,46].

X-ray photoelectron spectra (XPS) were further performed to provide more evidence of the chemical interaction between the *Pc* molecules and perovskite. As exhibited in Fig. 2d and 2e, the ZnPc and H_2Pc treated perovskite films display the binding energies of Pb (Pb 4f7/2, Pb 4f5/2) and I (I 3d5/2, I 3d3/2) are shifted to lower positions than those in control film (0.22 and 0.22 eV for Pb 4f and I 3d in ZnPc-treated sample, and 0.72 and 0.58 eV for Pb 4f and I 3d in H_2Pc-treated sample). Considering that simple physical mixing could not induce the chemical state changes, the binding energy shifts could be attributed to the coordination interaction between *Pc* molecules and unsaturated Pb on perovskite films, as we expected. The H_2Pc passivated sample shows the larger binding energy shift which is ascribed to the higher negative charge density on pyrrolic nitrogen in H_2Pc molecules, and the larger shift suggests the stronger chemical interaction between the H_2Pc molecules and uncoordinated Pb^{2+} ions than that of ZnPc-treated sample [13,47]. These results are in good accordance with the passivation mechanism we proposed. The XPS core energy level spectra of N 1 s and O 1 s were also provided in Fig. S4. As shown in Fig. S4a, the N 1 s spectrum of the H_2Pc-treated perovskite shows a peak of pyrrole N at 402.5 eV which is attributed to the H_2Pc molecule [48]. And the ZnPc-treated perovskite shows the peaks of pyrrole N and Zn-N at 402.5 eV and 400.2 eV, respectively, corresponding to the characteristic signal of ZnPc molecule [49,50]. The N 1 s spectra give strong evidence that the ZnPc and H_2Pc exist on the surface of perovskite film. And the O 1 s peaks around 532.8 eV shown in Fig. S4b are associated with adsorbed oxygen and moisture [51]. The decreased peak intensity indicates that the *Pc* treatments can reduce the invasion of moisture and oxygen. As illustrated by the C 1 s spectra in Fig. 2f, all the perovskite samples show two peaks at 286.0 eV and 284.8 eV, which are assigned to C—N and C—C [52], respectively. Note that the C—C is assigned to adventitious carbon or other contamination. And the spectra of the modified sample show a noticeably increased area of the C—N peaks, which can be assigned to the C atoms from *Pc* molecules. Meanwhile, an evident C═O peak around 288.6 eV is detected in the pristine sample but not present in the modified sample, further demonstrating that that the *Pc* treatments can effectively protect the perovskite from oxygen and moisture and slow the degradation in ambient air. Raman spectrum is also used to analyze the chemical interaction. As shown in Fig. S4c, the peaks at 68 cm^{-1} correspond to Pb-O stretching [53], and the peaks at 92 cm^{-1} are attributed to the *N*-C═N structure in *Pc* molecules [54]. The peaks at 107 cm^{-1}-113 cm^{-1} are assigned to the coupling mode of the PbI_6 octahedron and cation vibration [50]. The blueshifts from 107 cm^{-1} to 111 cm^{-1} or 113 cm^{-1} reflect the changes in lattice vibrations, which are induced by the chemical interaction. Moreover, two new peaks appear at 137 cm^{-1} and 130 cm^{-1}, providing direct evidence of the formed coordination bonding between N atoms and uncoordinated Pb ions [55].

To investigate the effects of *Pc* molecules treatments on the surface morphology of perovskite thin films, scanning electron microscopy

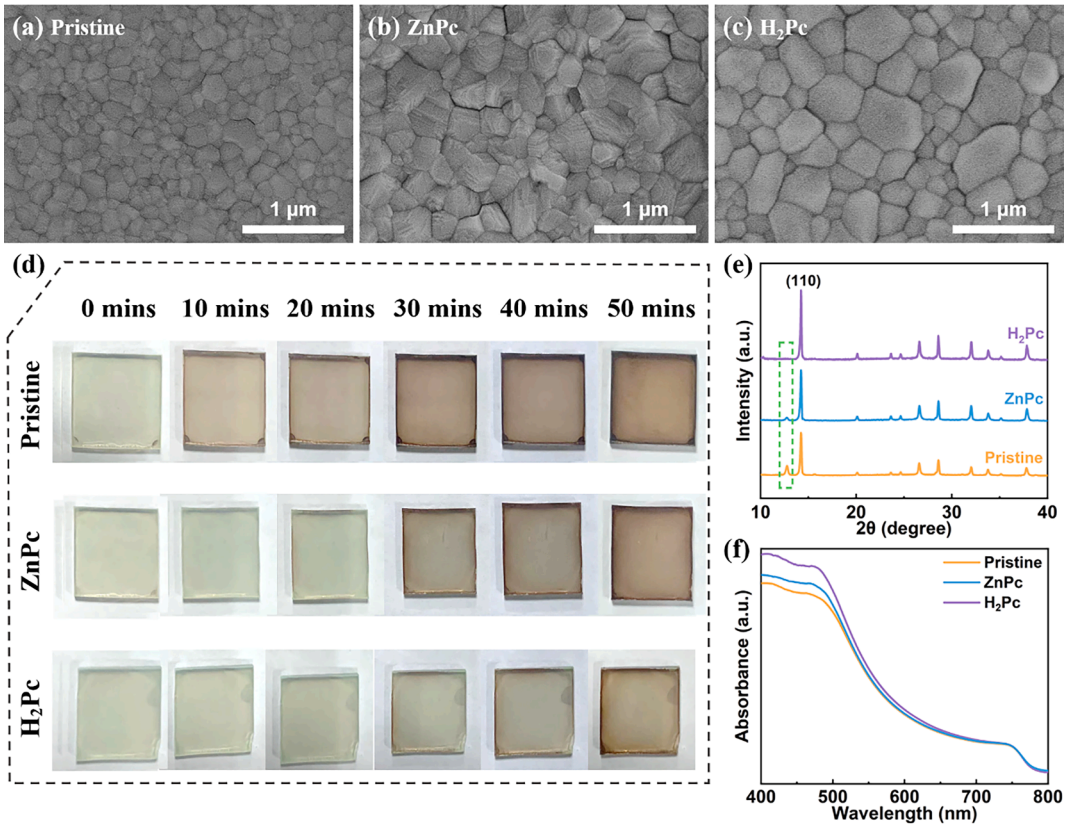

Fig. 3. Top-view SEM images of (a) pristine perovskite, (b) ZnPc treated perovskite and (c) H_2Pc treated perovskite. (d) Color evolution of perovskite precursor films without annealing. (e) XRD patterns and (f) UV–vis absorption spectra of perovskite samples.

(SEM) images were collected. As presented in Fig. 3a–c, the qualities and grain sizes of the perovskite films are significantly improved by ZnPc and H_2Pc treatments and the H_2Pc treated perovskite film exhibits the best film quality and the largest grain size. The abundant grain boundary resulted by the small grain size is harmful to charge transfer, and induces non-radiative recombination, leading to a reduction of photovoltaic performance. To quantitatively analyze the grain size, the enlarged SEM images are obtained as shown in Fig. S5a–c, and the corresponding grain size statistical distribution is shown in Fig. S5d–f. It is worth noting that the H_2Pc-treated perovskite exhibits a more uniform and dense film with an enlarged grain size mainly in the ranges of 300–600 nm. The cross-sectional SEM images of the samples shown in Fig. S5g–i further demonstrate the enlarged grain size by ZnPc and H_2Pc treatments. The improved film quality is attributed that the *Pc* molecules as Lewis base can slow down the crystallization process by the formation of chemical interaction with undercoordinated Pb^{2+}. To visually unveil the crystallization process, the substrates after spin-coating perovskite precursor (precursor films without annealing) were kept in ambient air at room temperature for 50 min. The color evolution of as-prepared precursor films is recorded as shown in Fig. 3d. We observed that it takes a longer time for precursor films turning from transparent to dark brown after the introduction of *Pc* molecules and the H_2Pc treated perovskite sample shows the slowest crystallization process. These results suggest that the introduction of *Pc* molecules slows down the solvent volatilization rate and prolongs the crystallization time. It has been reported that the crystallinity is mainly governed by nucleation and crystal growth, and the slowed crystal growth is conducive to improving the crystallinity of the perovskite films [56,57]. X-ray diffraction (XRD) measurements were conducted to investigate the crystal structure of perovskite films. As presented in Fig. 3e, all the samples show the typical diffraction peaks of $MAPbI_3$ perovskite films and the dominant peak at 14.23° is assigned to the characteristic (1 1 0) lattice planes [58]. Compared with the pristine sample, the ZnPc and H_2Pc treated perovskite samples show the increased (1 1 0) diffraction peak intensities and decreased full width at half maximum (FWHM, Fig. S6), and the PbI_2 peak at 12.76° is completely eliminated in H_2Pc treated sample. These results verify that the introduction of H_2Pc molecules effectively enhances the crystallinity of perovskite. Subsequently, the ultraviolet–visible (UV – vis) absorption spectra were also measured to investigate the impact of passivation molecules on light harvesting ability. As shown in Fig. 3f, both the samples without and with organic molecule treatments show a similar absorption profile and edge, suggesting that the organic molecule treatments give a negligible contribution to the band gap of perovskite. And the significantly improved absorption intensity in H_2Pc treated sample is attributed to the improved morphology and crystallinity of perovskite film.

Steady-state photoluminescence (PL) and time-resolved photoluminescence (TRPL) measurements were performed to evaluate the carrier recombination dynamics of perovskite films. To avoid the influence of charge injection from the light absorption layer to the transparent conducting oxide substrate, the perovskite films were prepared on the blank glass substrates. As shown in Fig. 4a, the PL intensities of passivated samples are significantly increased compared with the pristine perovskite, implying that the nonradiative recombination defects are effectively suppressed. In particular, the H_2Pc perovskite exhibits the highest radiative capacity, indicating that the H_2Pc molecules give the best passivation effect. Accompanying with the PL intensity increasement, blue shifts are observed in passivated samples, whereas the absorption edges remain unchanged, implying the suppressed band-tail state of perovskite by effective passivation [39]. The TRPL spectra reflect the similar results with steady-state PL spectra as presented in Fig. 4b. The decay curves are fitted by a biexponential model with Eq. (1) and the average decay times (τ_{ave}) are calculated according to Eq. (2):

$$y = A_1 e^{(-t/\tau_1)} + A_2 e^{(-t/\tau_2)} \quad (1)$$

$$\tau_{ave} = \left(A_1\tau_1^2 + A_2\tau_2^2\right)/\left(A_1\tau_1 + A_2\tau_2\right) \quad (2)$$

where A_1 and A_2 are decay amplitudes, τ_1 and τ_2 correspond to fast decay lifetimes and slow decay lifetimes, respectively, and the related fitting parameters are listed in Table S1. As expected, the ZnPc and H_2Pc perovskite shows higher τ_{ave} values than that of the pristine perovskite sample, which further demonstrates that the *Pc* treatments effectively suppress the defect-assisted recombination. Meanwhile, the PL and TRPL measurements were also used to investigate the interfacial charge

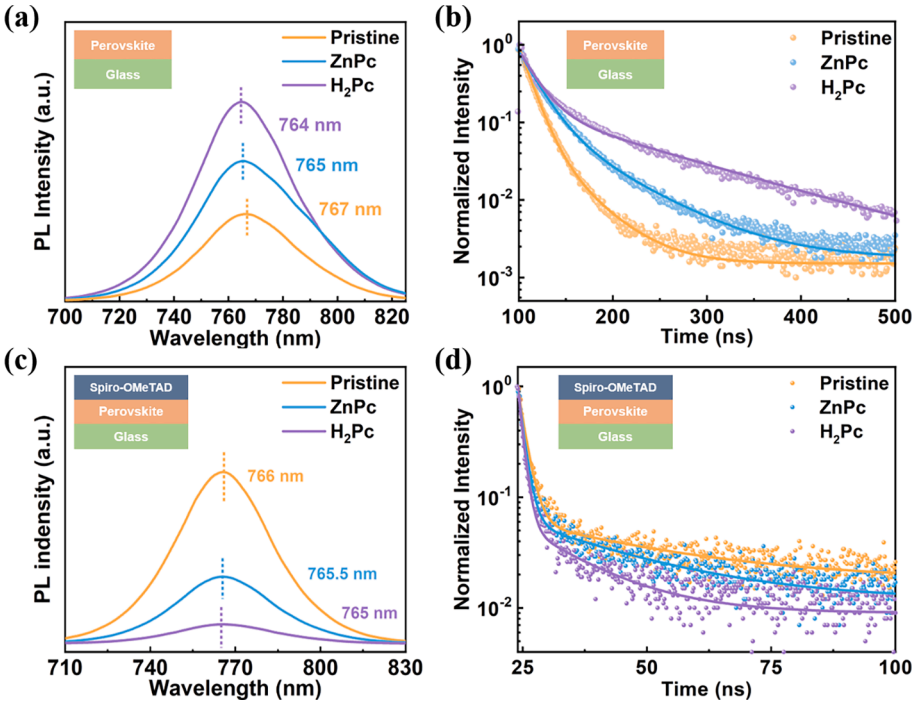

Fig. 4. (a) PL and (b) TRPL spectra of glass/perovskite samples. (c) PL and (d) TRPL spectra of glass/perovskite/SpiroOMeTAD samples.

carrier transfer by introducing hole transport layers. As seen from Fig. 4c, d, the H_2Pc perovskite exhibits the strongest fluorescence quenching and shortest decay lifetimes, suggesting that the hole extraction efficiency is remarkably improved. The significantly accelerated charge carrier transfer in the H_2Pc perovskite sample is attributed to the simultaneous defect passivation and improved energy level alignment, in agreement with the results discussed before.

To evaluate the effects of *Pc* treatments on photovoltaic performances, the current density–voltage (J-V) performance of the devices was assessed under AM 1.5G simulated solar light (100 mW cm^{-2}) condition. To maximize the passivation effects, the concentration of *Pc* molecules in antisolvent was optimized. The J-V curves depending on the concentration of ZnPc and H_2Pc are presented in Fig. S7 and the relevant photovoltaic parameters are shown in Table S3 and S4. It is obviously observed that both ZnPc and H_2Pc devices show optimal performance at a concentration of 5×10^{-4} M. Hereafter, the data for both ZnPc and H_2Pc devices are based on this optimal concentration. The statistical distributions of photovoltaic parameters from 30 individual devices for each case are listed in Fig. 5a–d. The H_2Pc devices exhibit significantly increased PCE as a consequence of improved short-circuit current density (J_{sc}), open-circuit voltage (V_{oc}), and fill factor (FF) compared with the pristine and ZnPc devices. And all the devices exhibit a highly concentrated parameter distribution, which validates the reproducibility and reliability of the device performance. Fig. 5e presents J-V curves of the champion devices modified with ZnPc and H_2Pc, along with the pristine device, measured in reverse scan directions and the corresponding photovoltaic parameters are listed in Table S5. As displayed in Table S5, the devices for pristine and ZnPc give a PCE of 16.50 % with a Voc of 1.06 V, J_{sc} of 21.37 mA cm^{-2}, and FF of 72.82 % and a PCE of 18.54 %, with a V_{oc} of 1.10 V, J_{sc} of 22.44 mA cm^{-2}, and FF of 75.12 %, respectively. For comparison, the H_2Pc device shows a significantly enhanced PCE of 20.59 % with a V_{oc} of 1.13 V, a J_{sc} of 23.26 mA cm^{-2}, and FF of 78.34 %. The improved J_{sc} is ascribed to the improved quality of perovskite films and the enhancement of light absorbance ability. And the enhanced Voc and FF are ascribed to the inhibited nonradiative recombination resulted from effective interface defect passivation and reduced interface energy barrier induced by improved energy level alignment. Moreover, the horizontally aligned *Pc* molecules on the perovskite layer may also give a positive effect on the photovoltaic performance since the *Pc* molecules can serve as an interfacial linker between perovskite and HTL. The link to the perovskite is achieved by coordination interaction and the link to the HTL is achieved through π-π conjugation interactions [22,59]. The external quantum efficiency (EQE) spectra and the integrated J_{sc} curves are presented in Fig. 5f. The calculated integrated J_{sc} values from the EQE spectra are close to the J–V curves, which demonstrates the reliability of the photovoltaic measurements. As exhibited in Fig. 5g and 5 h, the notorious J-V hysteresis phenomena are significantly alleviated by H_2Pc treatment, which originates from the reduced trap densities and suppressed ion migration and inner capacitive effects [60–62]. The steady-state power outputs at the maximum power point are recorded as 15.93 %, 18.07 % and 20.09 % for the pristine, ZnPc and H_2Pc devices, respectively (Fig. 5i), which match well with J-V results.

To further elucidate the photovoltaic characteristics, the J − V curves of pristine and H_2Pc devices are further analyzed based on the single heterojunction solar cell theory [63–65] and the detailed processes are

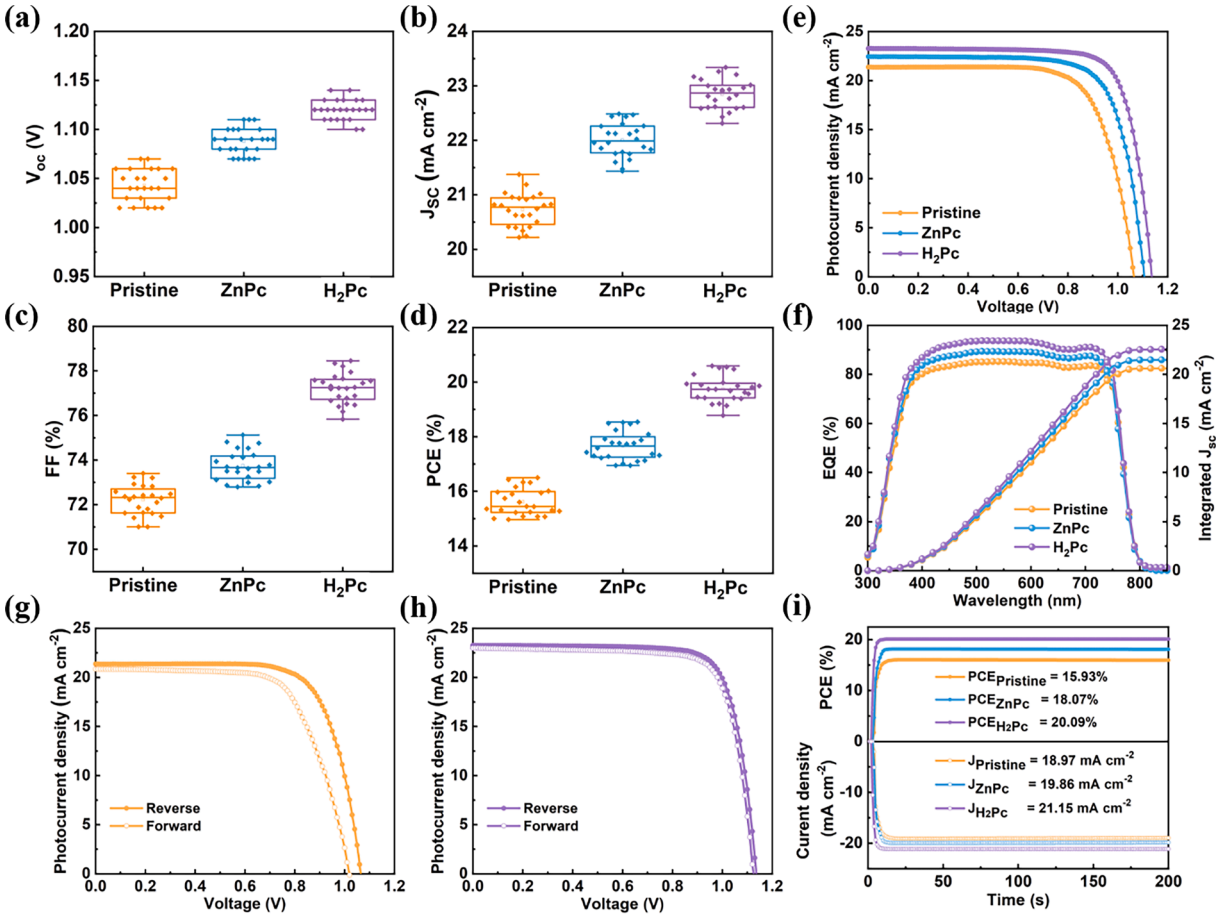

Fig. 5. Statistical distributions of photovoltaic parameters (a) V_{oc}, (b) J_{sc}, (c) FF, and (d) PCE. (e) J-V curves measured in reverse scan directions and (f) EQE spectra along with integrated J_{sc} curves of best performing ZnPc and H_2Pc devices as well as the pristine device. The J–V curves of (g) pristine device and (h) H_2Pc device measured in reverse and forward scan directions. (i) The steady-state photocurrent and PCE outputs at maximum power point for the pristine, ZnPc and H_2Pc devices.

presented in Supporting Information. The values of series resistance (R_s) and reverse saturated current density (J_0) can be extracted from the intercepts of linear fitting of the $-dV/dJ$ vs $(J_{sc}-J)^{-1}$ and $\ln(J_{sc}-J)$ vs $(V+R_sJ)$ plots, respectively. As shown in Fig. 6a and 6b, the values of R_s are 1.75 and 0.35 Ω cm^2 for the pristine and H_2Pc devices, respectively, while the corresponding J_0 is determined to be 1.10×10^{-5} and 5.29×10^{-6} mA/cm^2. A lower R_s represents less energy loss and better charge transport. J_0 represents the thermal emission rate of electrons from the valence band to the conduction band, which is closely related to carrier recombination. The reduced J_0 indicates lower carrier recombination, leading to the increasement of V_{oc} and FF. As depicted in Fig. S9, the H_2Pc device exhibits the lowest dark current density, which indicates the suppressed carrier recombination and improved charge extraction. To quantitatively evaluate the effects of *Pc* molecules on trap density, space charge limited current (SCLC) measurements were carried out. The dark J-V curves of the electron-only devices with a structure of glass/FTO/TiO_2/perovskite/PCBM/Ag are shown in Fig. 6c. The linear region at low bias voltage directly relates to the applied electric field, corresponding to the ohmic response. As the voltage increases, the current density shows a nonlinear increase, which is defined as the trap-filled limit (TFL) region. The kink point of the bias voltage between the ohmic region and TFL region is defined as the trap-filled limit voltage (V_{TFL}). And the trap density (N_t) can be calculated according to the following equation:

$$N_t = \frac{2\varepsilon_0\varepsilon V_{TFL}}{eL^2} \tag{3}$$

where L is the thickness of the perovskite film, ε_0 is the vacuum permittivity, and ε is the relative dielectric constant of the perovskite film. The N_t values for pristine, ZnPc and H_2Pc samples calculated to be $1.32\times10^{16}cm^{-3}$, $8.69\times10^{15}cm^{-3}$ and $7.91\times10^{15}cm^{-3}$, respectively. The extremely reduced trap density is attributed to the reduced interfacial charge recombination and improved film quality by *Pc* molecules modification. To further analyze the influence of *Pc* molecules treatments on the interfacial carrier recombination and charge transfer, electrochemical impedance spectroscopy (EIS) measurements were conducted. The impedance spectra were measured at different applied voltages in the dark condition, and the corresponding equivalent circuit model is presented in the inset of Fig. S10. As shown in Fig. 6d, the recombination resistance (R_{rec}) was much increased after the H_2Pc treatment for all the investigated applied voltages, which suggests the effectively suppressed charge recombination, thus resulting in the improvement in V_{oc}. The Nyquist plots of the samples obtained at a bias of 0.9 V are presented in Fig. S10. The H_2Pc device exhibits a reduced charge transfer resistance (R_{ct}), which suggests the enhanced charge transfer ability, leading to an improvement of J_{sc}. These EIS results are in extraordinary accordance with the above PL and TRPL analysis, demonstrating that H_2Pc treatment can effectively reduce interfacial non-radiative recombination losses by effective defect passivation. The frequency-dependent capacitance (Fig. 6e) represents ion accumulation at the interfaces of the devices, the decreased capacitance of H_2Pc device suggests the suppressed ion accumulation, which is originated from lower trap density and related to the reduction of hysteresis effect [66]. The Mott − Schottky analysis is also conducted to evaluate the built-in voltage (V_{bi}) of the devices by capacitance–voltage (C-V) measurements using the following equation:

$$C^{-2} = \frac{2(V_{bi}-V)}{A^2q\varepsilon_0\varepsilon N_A} \tag{4}$$

where A represents the active area, N_A represents the charge density and V represents the applied bias. As shown in Fig. 6f, it is observed that the H_2Pc device exhibits higher slope and higher V_{bi} value than that of pristine and ZnPc samples, implying the reduced carrier accumulation and enhanced driving force of carrier transfer and accounts for the obviously improved V_{oc}.

As a crucial part of PSCs technology, stability is an important indicator for the evaluations of practical applications. The stability of the perovskite films and corresponding devices is systematically investigated. As shown in Fig. 7a, the H_2Pc device retains over 90 % of its initial PCE after storage for 1000 h at dark in the ambient atmosphere about 20 % relative humidity (RH) and room temperature, while the pristine and ZnPc drops to 65 % and 76 % of their initial PCE, respectively. In general, the formation of PbI_2 is one of the key signs of $MAPbI_3$ perovskite decomposition. Thus, XRD measurements of the corresponding

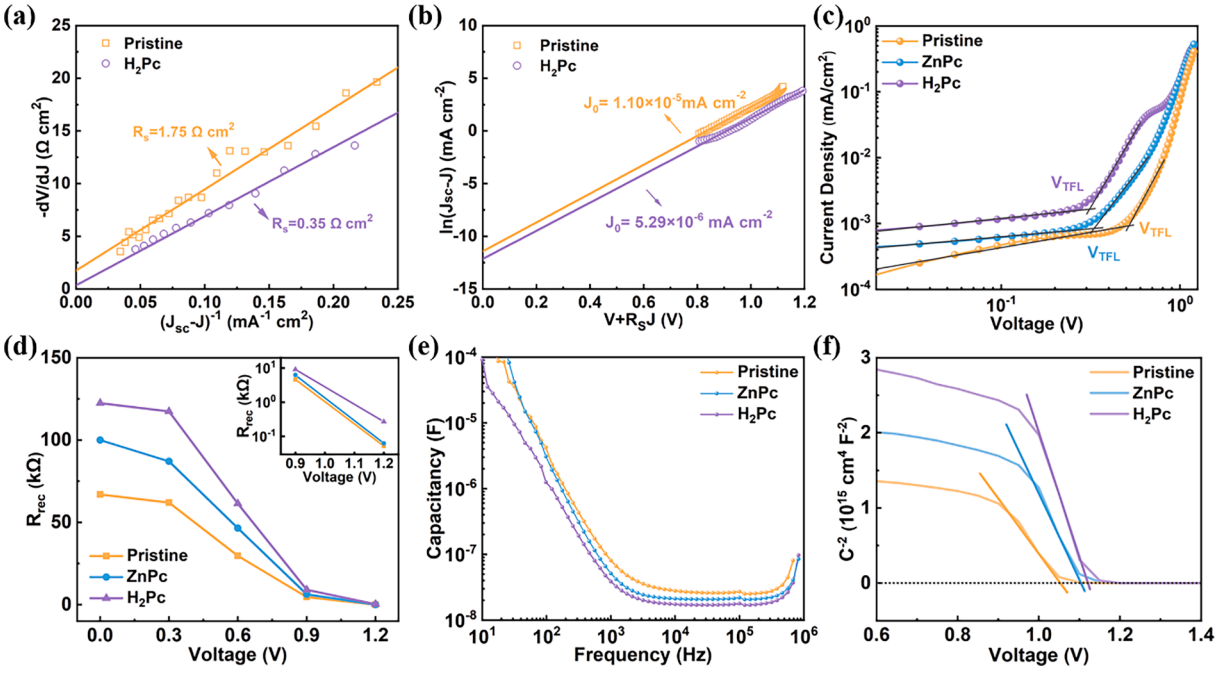

Fig. 6. Plots of the relationship of (a) $-dV/dJ$ vs $(J_{sc}-J)^{-1}$ and (b) $\ln(J_{sc}-J)$ vs $(V+R_sJ)$ for pristine and H_2Pc device, respectively. (c) Dark J-V curves for the electron-only devices of SCLC measurements. (d) Recombination resistances by fitting Nyquist plots dependence of bias voltages. (e) The capacitance-frequency response curves. (f) The Mott − Schottky plots.

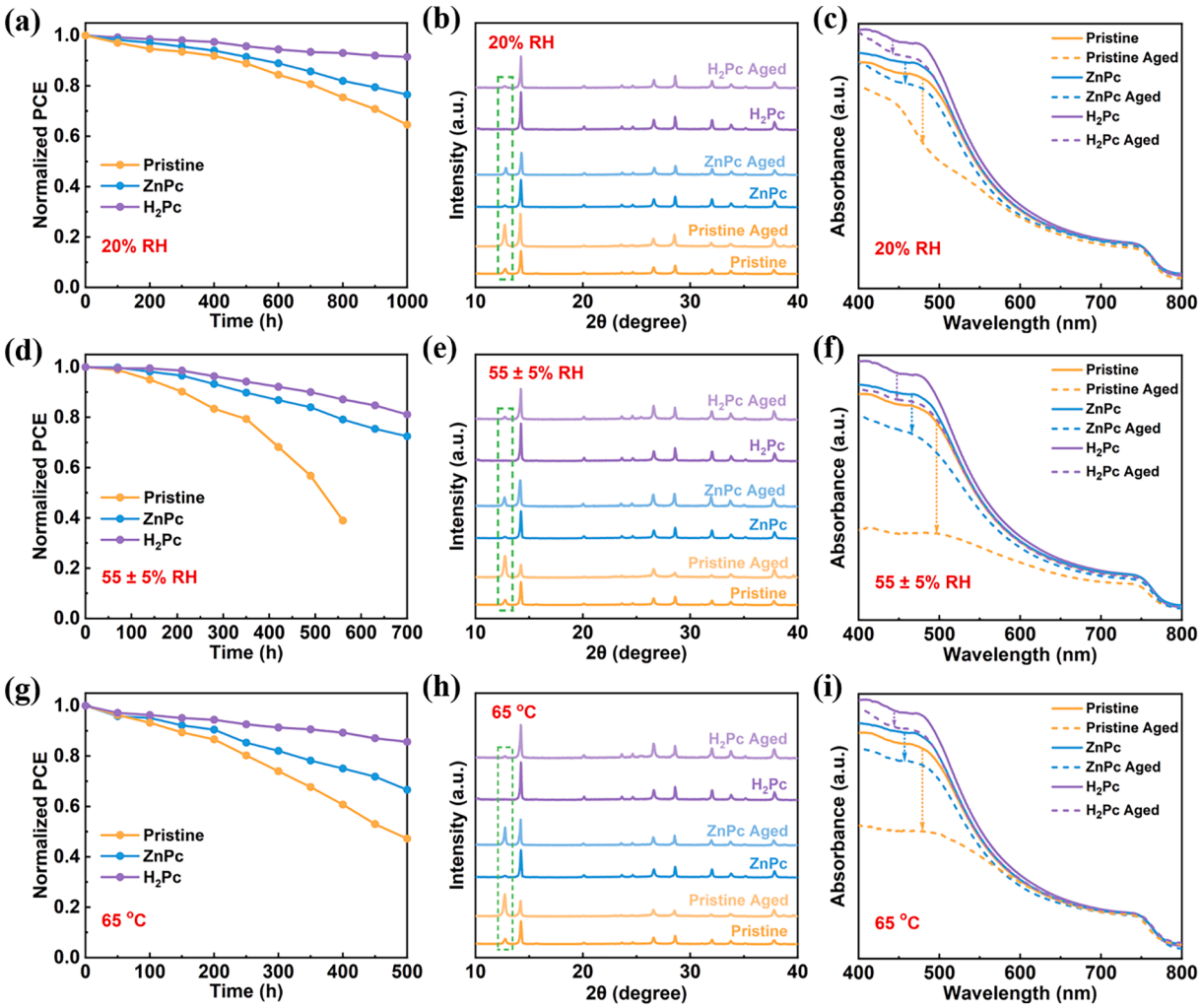

Fig. 7. The evolution of (a) PCE of the unencapsulated devices, (b) XRD patterns and (c) UV–vis absorption spectra of the perovskite films samples after storage for 1000 h at dark in the ambient atmosphere about 20 % RH and room temperature. The evolution of (d) PCE of the unencapsulated devices, (e) XRD patterns and (f) UV–vis absorption spectra of the perovskite films samples after storage for 700 h under 55 ± 5 % RH environment. The evolution of (g) PCE of the unencapsulated devices, (h) XRD patterns and (i) UV–vis absorption spectra of the perovskite films samples after storage for 500 h at 65 °C.

perovskite films were conducted under the same conditions aging for 1000 h. It is observed that obvious PbI_2 peaks appear in pristine and ZnPc-treated perovskite film but are hardly identified in H_2Pc perovskite film (Fig. 7b). The UV–vis absorption spectra are also utilized to assess the stability performance. As shown in Fig. 7c, the H_2Pc perovskite film exhibits a less light absorption decay than that of pristine and ZnPc samples. These results prove that the H_2Pc treatment can effectively improve the storage stability of perovskite films and the corresponding device. The significantly enhanced long-term stability encourages us to continue to explore the humidity stability and thermal stability. For moisture stability and thermal stability measurements, the performances of PSCs were tracked under the condition of 55 ± 5 % RH and 65 °C environments, respectively. As shown in Fig. 7d, the H_2Pc and ZnPc devices still preserve over 80 % and 70 % of their original PCE under moisture stress for 700 h, yet the pristine device lost most of its performance. The obviously improved moisture stability is benefited from the hydrophobicity property of *Pc* molecules, which is also proved by the water contact angle measurements, as shown in Fig. S11. Meanwhile, the improved moisture stability is also reflected by the XRD (Fig. 7e) and UV–vis absorption spectra (Fig. 7f). After aging for 500 h at 65 °C, the H_2Pc device maintains 86 % of the initial PCE, while the pristine and ZnPc devices drop to 47 % and 67 % of their original PCE, respectively (Fig. 7g). The thermal stability of the perovskite films was also investigated by XRD (Fig. 7h) and UV–vis absorption spectra (Fig. 7i), which shows the identical variation trend with the evolution of PCE. The significantly improved thermal stability of perovskite is attributed to the superior thermal stability of the *Pc* passivator and the reduction of defect density. The illumination stability measurements were also conducted under continuous AM 1.5 G illumination in ambient air. As shown in Fig. S12, the illumination stability of the devices is significantly improved by ZnPc and H_2Pc treatments and the H_2Pc device shows the best illumination stability. The H_2Pc device preserves over 80 % of their original PCE after 100 h continuous illumination. The improved illumination stability of perovskite films is also demonstrated by XRD and UV–vis absorption spectra measurements. It is worth noting that the H_2Pc device exhibited better performance than the ZnPc device, which is largely related to the formation of hydrogen bond, anchoring volatile iodine ions. Finally, the reasons for the excellent long-term stability of the H_2Pc device can be summarized as the following points: (1) The decreased defect densities, improved film quality, and suppressed ion migration derived from the passivation effect which slow down the decomposition rate. (2) The improved hydrophobic of perovskite films confirmed by the water contact angle measurements. (3) The superior thermal stability of the *Pc* passivator and the formed hydrogen bond between N—H and iodine ions which act as an iodine ion locker to stabilize perovskite.

3. Conclusions

In summary, we have demonstrated that the multifunctional metal-free H_2Pc molecule can simultaneously realize defect passivation, crystallinity optimization, energy level modulation, and improved stability of perovskite films. Compared with the metal ZnPc molecule, the H_2Pc molecule exhibits higher capability to passivate defect due to the structure of pyrrolic nitrogen and N—H bond. And the H_2Pc-treated perovskite exhibits a better valence band alignment to SpiroOMeTAD hole transport layer. The defect passivation is achieved by the simultaneous formation of coordination bonding and hydrogen bonding between H_2Pc molecule and perovskite. And the crystallinity optimization is achieved by the slowed crystal growth velocity via H_2Pc molecule treatment. Furthermore, the hydrophobic and thermally stable properties of the phthalocyanine materials brings a significant increasement in the stability of PSCs against moisture and thermal degradation. As a result, the H_2Pc device exhibits a strikingly improved PCE of 20.59 % along with excellent long-term stability. Consequently, the present work provides a practical and efficient method to simultaneously passivate defects, modulate energy level, and improve crystallinity and stability of perovskite materials, and toward the purpose of realizing efficient and stable PSCs.

Declaration of Competing Interest

The authors declare that they have no known competing financial interests or personal relationships that could have appeared to influence the work reported in this paper.

Data availability

Data will be made available on request.

Acknowledgements

This work was financially supported by National Natural Science Foundation of China (Grant No. 22172154, 51872281, and 62075217), project funded by China Postdoctoral Science Foundation (Grant No. 2021TQ0357) and Jilin Provincial Department of Science and Technology (Grants 20210101148JC).

Appendix A. Supplementary data

Supplementary data to this article can be found online at https://doi.org/10.1016/j.cej.2023.141573.

References

[1] D.P. McMeekin, G. Sadoughi, W. Rehman, G.E. Eperon, M. Saliba, M. T. Hoerantner, A. Haghighirad, N. Sakai, L. Korte, B. Rech, M.B. Johnston, L. M. Herz, H.J. Snaith, A Mixed-cation lead mixed-halide perovskite absorber for tandem solar cells, Science 351 (6269) (2016) 151–155, https://doi.org/10.1126/science.aad5845.

[2] A. Miyata, A. Mitioglu, P. Plochocka, O. Portugall, J.T.W. Wang, S.D. Stranks, H. J. Snaith, R.J. Nicholas, Direct measurement of the exciton binding energy and effective masses for charge carriers in organic-inorganic tri-halide perovskites, Nat. Phys. 11 (7) (2015) 582–U94, https://doi.org/10.1038/nphys3357.

[3] M. Zhang, M. Ye, W. Wang, C. Ma, S. Wang, Q. Liu, T. Lian, J. Huang, Z. Lin, Synergistic cascade carrier extraction via dual interfacial positioning of ambipolar black phosphorene for high-efficiency perovskite solar cells, Adv. Mater. 32 (28) (2020) 2000999, https://doi.org/10.1002/adma.202000999.

[4] P. Qin, T. Wu, Z. Wang, L. Xiao, L. Ma, F. Ye, L. Xiong, X. Chen, H. Li, X. Yu, G. Fang, Grain boundary and interface passivation with core-shell au@cds nanospheres for high-efficiency perovskite solar cells, Adv. Funct. Mater. 30 (12) (2020) 1908408, https://doi.org/10.1002/adfm.201908408.

[5] National Renewable Energy Laboratory, Best Research-Cell Effciencies Chart, https://www.nrel.gov/pv/cell-efficiency.html.

[6] A. Kojima, K. Teshima, Y. Shirai, T. Miyasaka, Organometal halide perovskites as visible-light sensitizers for photovoltaic cells, J. Am. Chem. Soc. 131 (17) (2009) 6050–6051, https://doi.org/10.1021/ja809598r.

[7] M. Kim, J. Jeong, H.Z. Lu, T.K. Lee, F.T. Eickemeyer, Y.H. Liu, I.W. Choi, S.J. Choi, Y. Jo, H.B. Kim, S.I. Mo, Y.K. Kim, H. Lee, N.G. An, S. Cho, W.R. Tress, S. M. Zakeeruddin, A. Hagfeldt, J.Y. Kim, M. Gratzel, D.S. Kim, Conformal quantum dot-sno_2 layers as electron transporters for efficient perovskite solar cells, Science 375 (6578) (2022) 302–306, https://doi.org/10.1126/science.abh1885.

[8] S. Yang, S. Chen, E. Mosconi, Y. Fang, X. Xiao, C. Wang, Y. Zhou, Z. Yu, J. Zhao, Y. Gao, F. De Angelis, J. Huang, Stabilizing halide perovskite surfaces for solar cell operation with wide-bandgap lead oxysalts, Science 365 (6452) (2019) 473–478, https://doi.org/10.1126/science.aax3294.

[9] P. You, G. Tang, J. Cao, D. Shen, T.W. Ng, Z. Hawash, N. Wang, C.K. Liu, W. Lu, Q. Tai, Y. Qi, C.S. Lee, F. Yan, 2D Materials for conducting holes from grain boundaries in perovskite solar cells, Light Sci Appl 10 (1) (2021) 68, https://doi.org/10.1038/s41377-021-00515-8.

[10] L. Xiao, Z. Wang, C. Shi, X. Yu, L. Ma, H. Li, G. Fang, P. Qin, Simple ball-milled molybdenum sulfide nanosheets for effective interface passivation with self-repairing function to attain high-performance perovskite solar cells, Sol. RRL 6 (8) (2022) 2200061, https://doi.org/10.1002/solr.202200061.

[11] Z. Wang, C. Shi, Z. Wang, L. Xiao, T. Wu, X. Yu, L. Ma, X. Chen, J. Zhang, H. Lei, P. Qin, Solution-processed $fe_{2-x}mg_xo_3$ ternary oxides for interface passivation in efficient perovskite solar cells, Chem. Eng. J. 441 (2022), 136118, https://doi.org/10.1016/j.cej.2022.136118.

[12] Y. Ge, F. Ye, M. Xiao, H. Wang, C. Wang, J. Liang, X. Hu, H. Guan, H. Cui, W. Ke, C. Tao, G. Fang, Internal encapsulation for lead halide perovskite films for efficient and very stable solar cells, Adv. Energy Mater. 12 (19) (2022) 2200361, https://doi.org/10.1002/aenm.202200361.

[13] J. Guo, J. Sun, L. Hu, S. Fang, X. Ling, X. Zhang, Y. Wang, H. Huang, C. Han, C. Cazorla, Y. Yang, D. Chu, T. Wu, J. Yuan, W. Ma, Indigo: a natural molecular passivator for efficient perovskite solar cells, Adv. Energy Mater. 12 (22) (2022) 2200537, https://doi.org/10.1002/aenm.202200537.

[14] Z. Zhang, Y. Gao, Z. Li, L. Qiao, Q. Xiong, L. Deng, Z. Zhang, R. Long, Q. Zhou, Y. Du, Z. Lan, Y. Zhao, C. Li, K. Mullen, P. Gao, Marked passivation effect of naphthalene-1,8-dicarboximides in high-performance perovskite solar cells, Adv. Mater. 33 (31) (2021) 2008405, https://doi.org/10.1002/adma.202008405.

[15] G. Chen, P. Li, T. Xue, M. Su, J. Ma, Y. Zhang, T. Wu, L. Han, M. Aldamasy, M. Li, Z. Li, J. Ma, S. Chen, Y. Zhao, F. Wang, Y. Song, Design of low bandgap $cspb_{(1-x)}sn_xi_2br$ perovskite solar cells with excellent phase stability, Small 17 (30) (2021) e2101380.

[16] N. Li, S. Tao, Y. Chen, X. Niu, C.K. Onwudinanti, C. Hu, Z. Qiu, Z. Xu, G. Zheng, L. Wang, Y. Zhang, L. Li, H. Liu, Y. Lun, J. Hong, X. Wang, Y. Liu, H. Xie, Y. Gao, Y. Bai, S. Yang, G. Brocks, Q. Chen, H. Zhou, Cation and anion immobilization through chemical bonding enhancement with fluorides for stable halide perovskite solar cells, Nat. Energy 4 (5) (2019) 408–415, https://doi.org/10.1038/s41560-019-0382-6.

[17] C. Liang, P. Li, Y. Zhang, H. Gu, Q. Cai, X. Liu, J. Wang, H. Wen, G. Shao, Mild solution-processed metal-doped tio_2 compact layers for hysteresis-less and performance-enhanced perovskite solar cells, J. Power Sources 372 (2017) 235–244, https://doi.org/10.1016/j.jpowsour.2017.10.079.

[18] B. Wang, J. Ma, Z. Li, G. Chen, Q. Gu, S. Chen, Y. Zhang, Y. Song, J. Chen, X. Pi, X. Yu, D. Yang, Bioinspired molecules design for bilateral synergistic passivation in buried interfaces of planar perovskite solar cells, Nano Res. 15 (2) (2021) 1069–1078, https://doi.org/10.1007/s12274-021-3600-z.

[19] N. De Marco, H. Zhou, Q. Chen, P. Sun, Z. Liu, L. Meng, E.P. Yao, Y. Liu, A. Schiffer, Y. Yang, Guanidinium: a route to enhanced carrier lifetime and open-circuit voltage in hybrid perovskite solar cells, Nano Lett. 16 (2) (2016) 1009–1016, https://doi.org/10.1021/acs.nanolett.5b04060.

[20] J. Zang, C. Zhang, Y. Qiang, Q. Liu, Y. Fei, Z. Yu, Efficient and stable planar $mapbi_3$ perovskite solar cells based on a small molecule passivator, Surf. Interfaces 25 (2021), 101213, https://doi.org/10.1016/j.surfin.2021.101213.

[21] Z. Li, P. Li, G. Chen, Y. Cheng, X. Pi, X. Yu, D. Yang, L. Han, Y. Zhang, Y. Song, Ink Engineering of inkjet printing perovskite, ACS Appl Mater Interfaces 12 (35) (2020) 39082–39091, https://doi.org/10.1021/acsami.0c09485.

[22] T.H. Han, J.W. Lee, C. Choi, S. Tan, C. Lee, Y. Zhao, Z. Dai, N. De Marco, S.J. Lee, S. H. Bae, Y. Yuan, H.M. Lee, Y. Huang, Y. Yang, Perovskite-polymer composite cross-linker approach for highly-stable and efficient perovskite solar cells, Nat Commun 10 (1) (2019) 520, https://doi.org/10.1038/s41467-019-08455-z.

[23] F.L. Cai, J.L. Cai, L.Y. Yang, W. Li, R.S. Gurney, H.N. Yi, A. Iraqi, D. Liu, T. Wang, Molecular engineering of conjugated polymers for efficient hole transport and defect passivation in perovskite solar cells, Nano Energy 45 (2018) 28–36, https://doi.org/10.1016/j.nanoen.2017.12.028.

[24] C. Fu, Z. Gu, Y. Tang, Q. Xiao, S. Zhang, Y. Zhang, Y. Song, From structural design to functional construction: amine molecules in high-performance formamidinium-based perovskite solar cells, Angew Chem Int Ed Engl 61 (19) (2022) e202117067.

[25] H. Zhu, J. Ma, P. Li, S. Zang, Y. Zhang, Y. Song, Low-dimensional sn-based perovskites: evolution and future prospects of solar cells, Chem 8 (11) (2022) 2939–2960, https://doi.org/10.1016/j.chempr.2022.07.027.

[26] E.A. Alharbi, A.Y. Alyamani, D.J. Kubicki, A.R. Uhl, B.J. Walder, A.Q. Alanazi, J. S. Luo, A. Burgos-Caminal, A. Albadri, H. Albrithen, M.H. Alotaibi, J.E. Moser, S. M. Zakeeruddin, F. Giordano, L. Emsley, M. Gratzel, Atomic-level passivation mechanism of ammonium salts enabling highly efficient perovskite solar cells, Nat. Commun. 10 (2019) 3008, https://doi.org/10.1038/s41467-019-10985-5.

[27] L. Yan, J. Ma, P. Li, S. Zang, L. Han, Y. Zhang, Y. Song, Charge-carrier transport in quasi-2d ruddlesden-popper perovskite solar cells, Adv Mater 34 (7) (2022) e2106822.

[28] J. Wu, Y. Fang, D.i. Zhang, S. Zhang, J. Wan, R. Wen, X. Zhou, N. Fu, Y. Lin, Efficient and stable perovskite solar cells based on a quasi-point-contact and rear-

reflection structure with 22.5% efficiency, J. Mater. Chem. A 9 (26) (2021) 14877–14887.
[29] D.Y. Son, J.W. Lee, Y.J. Choi, I.H. Jang, S. Lee, P.J. Yoo, H. Shin, N. Ahn, M. Choi, D. Kim, N.G. Park, Self-formed grain boundary healing layer for highly efficient $ch_3nh_3pbi_3$ perovskite solar cells, Nat. Energy 1 (2016) 16081, https://doi.org/10.1038/nenergy.2016.81.
[30] W.Q. Wu, Z.B. Yang, P.N. Rudd, Y.C. Shao, X.Z. Dai, H.T. Wei, J.J. Zhao, Y.J. Fang, Q. Wang, Y. Liu, Y.H. Deng, X. Xiao, Y.X. Feng, J.S. Huang, Bilateral alkylamine for suppressing charge recombination and improving stability in blade-coated perovskite solar cells, Sci. Adv. 5 (3) (2019), https://doi.org/10.1126/sciadv.aav8925.
[31] Y. Zhang, Q. Chen, H.S. Yang, D. Kim, I. Shin, B.R. Lee, J.H. Kim, D.K. Moon, K. H. Kim, S.H. Park, Water-repellent perovskites induced by a blend of organic halide salts for efficient and stable solar cells, ACS Appl Mater Interfaces 13 (28) (2021) 33172–33181, https://doi.org/10.1021/acsami.1c09093.
[32] B. Yang, J. Suo, F. Di Giacomo, S. Olthof, D. Bogachuk, Y. Kim, X. Sun, L. Wagner, F. Fu, S.M. Zakeeruddin, A. Hinsch, M. Gratzel, A. Di Carlo, A. Hagfeldt, Interfacial passivation engineering of perovskite solar cells with fill factor over 82% and outstanding operational stability on n-i-p architecture, ACS Energy Lett. 6 (11) (2021) 3916–3923, https://doi.org/10.1021/acsenergylett.1c01811.
[33] Q. Hu, E. Rezaee, W. Xu, R. Ramachandran, Q. Chen, H. Xu, T. El-Assaad, D. V. McGrath, Z.X. Xu, Dual defect-passivation using phthalocyanine for enhanced efficiency and stability of perovskite solar cells, Small 17 (1) (2021) 2005216, https://doi.org/10.1002/smll.202005216.
[34] J. Cao, C. Li, X. Lv, X. Feng, R. Meng, Y. Wu, Y. Tang, Efficient grain boundary suture by low-cost tetra-ammonium zinc phthalocyanine for stable perovskite solar cells with expanded photoresponse, J. Am. Chem. Soc. 140 (37) (2018) 11577–11580, https://doi.org/10.1021/jacs.8b07025.
[35] H. Kim, K.S. Lee, M.J. Paik, D.Y. Lee, S.-U. Lee, E. Choi, J.S. Yun, S.I. Seok, Polymethyl methacrylate as an interlayer between the halide perovskite and copper phthalocyanine layers for stable and efficient perovskite solar cells, Adv. Funct. Mater. 32 (13) (2022) 2110473.
[36] G. Qu, L. Dong, Y. Qiao, D. Khan, Q. Chen, P. Xie, X. Yu, X. Liu, Y. Wang, J. Chen, X. Chen, Z.-X. Xu, Dopant-free phthalocyanine hole conductor with thermal-induced holistic passivation for stable perovskite solar cells with 23% efficiency, Adv. Funct. Mater. 32 (41) (2022) 2206585, https://doi.org/10.1002/adfm.202206585.
[37] S. Zhang, Z. Hu, J. Zhang, X. Jia, J. Jiang, Y. Chen, B. Lin, H. Jiang, B. Fang, N. Yuan, J. Ding, Interface engineering via phthalocyanine decoration of perovskite solar cells with high efficiency and stability, J. Power Sources 438 (2019), 226987, https://doi.org/10.1016/j.jpowsour.2019.226987.
[38] S. Jin, Y. Wei, F. Huang, X. Yang, D. Luo, Y. Fang, Y. Zhao, Q. Guo, Y. Huang, J. Wu, Enhancing the perovskite solar cell performance by the treatment with mixed anti-solvent, J. Power Sources 404 (2018) 64–72, https://doi.org/10.1016/j.jpowsour.2018.10.008.
[39] X. Gu, W. Xiang, Q. Tian, S.F. Liu, Rational surface-defect control via designed passivation for high-efficiency inorganic perovskite solar cells, Angew. Chem. Int. Ed. Engl. 60 (43) (2021) 23164–23170, https://doi.org/10.1002/anie.202109724.
[40] R. Wang, J. Xue, K.-L. Wang, Z.-K. Wang, Y. Luo, D. Fenning, G. Xu, S. Nuryyeva, T. Huang, Y. Zhao, J.L. Yang, J. Zhu, M. Wang, S. Tan, I. Yavuz, K.N. Houk, Y. Yang, Constructive molecular configurations for surface-defect passivation of perovskite photovoltaics, Science 366 (6472) (2019) 1509–1513, https://doi.org/10.1126/science.aay9698.
[41] C. Yang, H. Wang, Y. Miao, C. Chen, M. Zhai, Q. Bao, X. Ding, X. Yang, M. Cheng, Interfacial molecular doping and energy level alignment regulation for perovskite solar cells with efficiency exceeding 23%, ACS Energy Lett. 6 (8) (2021) 2690–2696, https://doi.org/10.1021/acsenergylett.1c01126.
[42] M. Jeong, I.W. Choi, E.M. Go, Y. Cho, M. Kim, B. Lee, S. Jeong, Y. Jo, H.W. Choi, J. Lee, J.-H. Bae, S.K. Kwak, D.S. Kim, C. Yang, Stable perovskite solar cells with efficiency exceeding 24.8% and 0.3-v voltage loss, Science 369 (6511) (2020) 1615–1620, https://doi.org/10.1126/science.abb7167.
[43] X. Sun, L. Shi, Y. Zhang, H. Yuan, K. Zhang, L. Duan, Q. Li, Z. Huang, X. Ban, D. Zhang, Synergistic modification of benzimidazole and bromohexyl for highly efficient and stable perovskite solar cells, Chem. Eng. J. 453 (2023), 139698, https://doi.org/10.1016/j.cej.2022.139698.
[44] C. Liu, J. Zhang, L. Zhang, X. Zhou, Y. Liu, X. Wang, B. Xu, Bifunctional passivation through fluoride treatment for highly efficient and stable perovskite solar cells, Adv. Energy Mater. 12 (30) (2022) 2200945, https://doi.org/10.1002/aenm.202200945.
[45] S. Yang, J. Dai, Z.H. Yu, Y.C. Shao, Y. Zhou, X. Xiao, X.C. Zeng, J.S. Huang, Tailoring passivation molecular structures for extremely small open-circuit voltage loss in perovskite solar cells, J. Am. Chem. Soc. 141 (14) (2019) 5781–5787, https://doi.org/10.1021/jacs.8b13091.
[46] X. Wang, W. Sun, Y. Tu, Q. Xiong, G. Li, Z. Song, Y. Wang, Y. Du, Q. Chen, C. Deng, Z. Lan, P. Gao, J. Wu, Lansoprazole, a cure-four, enables perovskite solar cells efficiency exceeding 24%, Chem. Eng. J. 446 (2022), 137416 https://doi.org/10.1016/j.cej.2022.137416.
[47] C. Tian, Y. Zhao, X. Han, B. Li, Y. Rui, H. Xiong, Y. Qiu, W. An, K. Li, C. Hou, Y. Li, H. Wang, Q. Zhang, All-in-one additive enables defect passivated, crystallization modulated and moisture resisted perovskite films toward efficient solar cells, Chem. Eng. J. 452 (2023), 139345, https://doi.org/10.1016/j.cej.2022.139345.
[48] B. Liu, H. Bi, D. He, L. Bai, W. Wang, H. Yuan, Q. Song, P. Su, Z. Zang, T. Zhou, J. Chen, Interfacial defect passivation and stress release via multi-active-site ligand anchoring enables efficient and stable methylammonium-free perovskite solar cells, ACS Energy Lett. 6 (7) (2021) 2526–2538, https://doi.org/10.1021/acsenergylett.1c00794.
[49] C. Xie, L. Lin, L. Huang, Z. Wang, Z. Jiang, Z. Zhang, B. Han, Zn-N_x sites on n-doped carbon for aerobic oxidative cleavage and esterification of C(CO)-C bonds, Nat Commun 12 (1) (2021) 4823, https://doi.org/10.1038/s41467-021-25118-0.
[50] X. Yang, Y. Ni, Y. Zhang, Y. Wang, W. Yang, D. Luo, Y. Tu, Q. Gong, H. Yu, R. Zhu, Multiple-defect management for efficient perovskite photovoltaics, ACS Energy Lett. 6 (7) (2021) 2404–2412, https://doi.org/10.1021/acsenergylett.1c01039.
[51] P. Wang, B. Chen, R. Li, S. Wang, Y. Li, X. Du, Y. Zhao, X. Zhang, 2D perovskite or organic material matter? targeted growth for efficient perovskite solar cells with efficiency exceeding 24%, Nano Energy 94 (2022), 106914 https://doi.org/10.1016/j.nanoen.2021.106914.
[52] K. Jung, W.-S. Chae, J.W. Choi, K.C. Kim, M.-J. Lee, Synergistic passivation of $mapbi_3$ perovskite solar cells by compositional engineering using acetamidinium bromide additives, J. Energy Chem. 59 (2021) 755–762, https://doi.org/10.1016/j.jechem.2020.12.022.
[53] P.L. Qin, G. Yang, Z.W. Ren, S.H. Cheung, S.K. So, L. Chen, J. Hao, J. Hou, G. Li, Stable and efficient organo-metal halide hybrid perovskite solar cells via π-conjugated lewis base polymer induced trap passivation and charge extraction, Adv Mater 30 (12) (2018) e1706126.
[54] J. Ibaceta-Jana, R. Muydinov, P. Rosado, H. Mirhosseini, M. Chugh, O. Nazarenko, D.N. Dirin, D. Heinrich, M.R. Wagner, T.D. Kuhne, B. Szyszka, M.V. Kovalenko, A. Hoffmann, Vibrational dynamics in lead halide hybrid perovskites investigated by raman spectroscopy, Phys Chem Chem Phys 22 (10) (2020) 5604–5614, https://doi.org/10.1039/c9cp06568g.
[55] Z. Wang, T. Wu, L. Xiao, P. Qin, X. Yu, L. Ma, L. Xiong, H. Li, X. Chen, Z. Wang, T. Wu, M.L. Xiao, P. Qin, D.X. Yu, D.L. Ma, D.L. Xiong, D.H. Li, X. Chen, Multifunctional potassium hexafluorophosphate passivate interface defects for high efficiency perovskite solar cells, J. Power Sources 488 (2021), 229451, https://doi.org/10.1016/j.jpowsour.2021.229451.
[56] D. Bi, C. Yi, J. Luo, J.-D. Décoppet, F. Zhang, S.M. Zakeeruddin, X. Li, A. Hagfeldt, M. Grätzel, Polymer-templated nucleation and crystal growth of perovskite films for solar cells with efficiency greater than 21%, Nat. Energy 1 (10) (2016) https://doi.org/10.1038/nenergy.2016.142.
[57] J. Tao, Z. Wang, H. Wang, J. Shen, X. Liu, J. Xue, H. Guo, G. Fu, W. Kong, S. Yang, Additive engineering for efficient and stable $mapbi_3$-perovskite solar cells with an efficiency of over 21%, ACS Appl Mater Interfaces 13 (37) (2021) 44451–44459, https://doi.org/10.1021/acsami.1c13136.
[58] W. Lv, Z. Hu, W. Qiu, D. Yan, M. Li, A. Mei, L. Xu, R. Chen, Constructing soft perovskite-substrate interfaces for dynamic modulation of perovskite film in inverted solar cells with over 6200 hours photostability, Adv. Sci. 9 (28) (2022) 2202028, https://doi.org/10.1002/advs.202202028.
[59] J. Urieta-Mora, I. Garcia-Benito, A. Molina-Ontoria, N. Martin, Hole transporting materials for perovskite solar cells: a chemical approach, Chem Soc Rev 47 (23) (2018) 8541–8571, https://doi.org/10.1039/c8cs00262b.
[60] X. Li, C.-C. Chen, M. Cai, X. Hua, F. Xie, X. Liu, J. Hua, Y.-T. Long, H.e. Tian, L. Han, Efficient passivation of hybrid perovskite solar cells using organic dyes with -cooh functional group, Adv. Energy Mater. 8 (20) (2018) 1800715.
[61] X. Lai, W. Li, X. Gu, H. Chen, Y. Zhang, G. Li, R. Zhang, D. Fan, F. He, N. Zheng, J. Yu, R. Chen, A.K.K. Kyaw, X.W. Sun, High-performance quasi-2d perovskite solar cells with power conversion efficiency over 20% fabricated in humidity-controlled ambient air, Chem. Eng. J. 427 (2022), 130949, https://doi.org/10.1016/j.cej.2021.130949.
[62] J. Chen, X. Zhao, S.G. Kim, N.G. Park, Multifunctional chemical linker imidazoleacetic acid hydrochloride for 21% efficient and stable planar perovskite solar cells, Adv Mater 31 (39) (2019) e1902902.
[63] T. Liu, P. Su, L. Liu, J. Wang, S. Feng, J. Zhang, R. Xu, H. Yang, W. Fu, An ionic compensation strategy for high-performance mesoporous perovskite solar cells: healing defects with tri-iodide ions in a solvent vapor annealing process, J. Mater. Chem. A 7 (1) (2019) 353–362, https://doi.org/10.1039/c8ta10094b.
[64] J. Shi, J. Dong, S. Lv, Y. Xu, L. Zhu, J. Xiao, X. Xu, H. Wu, D. Li, Y. Luo, Q. Meng, Hole-conductor-free perovskite organic lead iodide heterojunction thin-film solar cells: high efficiency and junction property, Appl. Phys. Lett. 104 (6) (2014) 063901.
[65] J. You, Y.(. Yang, Z. Hong, T.-B. Song, L. Meng, Y. Liu, C. Jiang, H. Zhou, W.-H. Chang, G. Li, Y. Yang, Moisture assisted perovskite film growth for high performance solar cells, Appl. Phys. Lett. 105 (18) (2014) 183902.
[66] J. Zhu, Y. Qian, Z. Li, O.Y. Gong, Z. An, Q. Liu, J.H. Choi, H. Guo, P.J. Yoo, D. H. Kim, T.K. Ahn, G.S. Han, H.S. Jung, defect healing in $fapb(i_{1-x}br_x)_3$ perovskites: multifunctional fluorinated sulfonate surfactant anchoring enables >21% modules with improved operation stability, Adv. Energy Mater. 12 (20) (2022) 2200632, https://doi.org/10.1002/aenm.202200632.